Analytic three-dimensional 'MLR' potential energy surface for CO_2–He, and its predicted microwave and infrared spectra†

Hui Li and Robert J. Le Roy*

Received 15th January 2008, Accepted 11th April 2008
First published as an Advance Article on the web 4th June 2008
DOI: 10.1039/b800718g

A three-dimensional, analytic potential energy surface for CO_2–He that explicitly incorporates its dependence on the Q_3 asymmetric-stretch normal-mode coordinate of the CO_2 monomer has been obtained by least-squares fitting new *ab initio* interaction energies to a new three-dimensional Morse/Long-Range (3D-MLR) potential function form. This fit to 2832 points has a root-mean-square (RMS) deviation of 0.032 cm^{-1} and requires only 55 parameters. The resulting pure *ab initio* potential provides a good representation of the experimental microwave and infrared data: for 51 pseudo microwave and 49 infrared transitions the RMS discrepancies are 0.0110 and 0.0445 cm^{-1}, respectively. Scaling this surface using only two morphing parameters yields an order of magnitude better agreement with experiments, with RMS discrepancies of only 0.0025 and 0.0038 cm^{-1}, respectively. The calculated infrared band origin shift associated with the ν_3 fundamental of CO_2 is 0.109 cm^{-1}, in good agreement with the (extrapolated) experimental value of 0.095 cm^{-1}.

I. Introduction

The CO_2–He complex is an interesting test case with respect to empirical[1–3] and *ab initio*[4–6] determination of intermolecular forces, because CO_2 is being used as a dopant molecule in helium cluster studies.[7–12] An accurate description of the binary complex is an essential starting point for exploration of larger clusters, as quantum Monte Carlo simulations of doped He clusters are known to be very sensitive to the quality of the pair potentials utilized for the simulations.[8,13] Since the first infrared spectrum of CO_2–He complexes in the region of the strong ν_3 fundamental band of CO_2 was recorded in 1994 by Weida *et al.*,[14] there have been three theoretical studies of this complex.[4–6] However, all predicted spectra were based on 2-D potential energy surfaces with CO_2 fixed at its equilibrium geometry, which may be an adequate approximation for describing microwave spectra of ground-state species, but not for infrared spectra involving excitation of an intramolecular CO_2 vibrational mode. The most recent *ab initio* potentials were obtained from MP4 or SAPT calculations,[4–6] and were fitted to an exponential-spline-Morse-Morse-Spline-Van der Waals[4] or repulsive-plus-attractive analytical forms.[5,6] The root mean square (RMS) discrepancies of those fits to the *ab initio* points ranged from 1.0 to 8.16 cm^{-1}.

Recently, Le Roy *et al.* introduced the "Morse/Long-Range" (MLR) radial potential function form which incorporates theoretically known long-range inverse-power behaviour and is a single smooth analytic function, rather than being made up of joined segments.[15,16] Allowing parameters of that radial function to vary with angle and with Q_3 yields a compact and flexible 3-D potential form that explicitly incorporates the Q_3 asymmetric-stretch vibrational motion of CO_2, and has the correct angle-dependent inverse-power long-range behaviour. This function is fitted to results of new high-level *ab initio* calculations, and used to predict the rovibrational eigenvalues of CO_2–He, both without and with separation of the inter- and intramolecular nuclear motions. The new *ab initio* calculations and the techniques used for computing the eigenvalues of the resulting potential energy surface are described in section II. Section III then presents our analytic 3-D potential function form and describes its fit to the *ab initio* data. Section IV then presents predictions of the infrared and microwave spectra for the He–CO_2 dimer implied by this surface, and shows that a very simple two-parameter morphing of the pure *ab initio* surface improves the agreement with experiment by almost an order of magnitude.

II. Computational methods

A *Ab initio* calculations

The geometry of a CO_2–He complex in which CO_2 is kept linear can be described naturally using Jacobi coordinates (R, θ, Q_3), where R is the distance from the center of mass of CO_2 to the He atom, θ the angle between the vector pointing from the center of mass of CO_2 to He and the vector pointing from one oxygen atom to the other, and Q_3 is the normal mode coordinate for the ν_3 antisymmetric stretch vibration of CO_2, which can be simply defined as

$$Q_3 = (r_{CO_{[1]}} - r_{CO_{[2]}})/\sqrt{2}, \quad (1)$$

where $r_{CO_{[1]}}$ and $r_{CO_{[2]}}$ are the two C–O bond lengths. In our *ab initio* calculations for the CO_2–He complex, the average of the

Department of Chemistry, University of Waterloo, Waterloo, Ontario, Canada N2L 3G1. E-mail: leroy@uwaterloo.ca

† Electronic supplementary information (ESI) available: Tables A-1 to A-7; an ASCII listing of the *ab initio* points defining the 3D potential energy surface; and ASCII listings of Fortran subroutines for generating both the 2D and 3D versions of the surfaces. See DOI: 10.1039/b800718g

two C–O bond lengths was fixed at the experimental vibrationally averaged ground state bond length, r_0 = 1.162086 Å.[17]

The intermolecular potential energies of CO_2–He were calculated using single- and double-excitation coupled-cluster theory with a non-iterative perturbation treatment of triple excitations [CCSD(T)].[18] The basis set used was the augmented correlation-consistent quadruple-zeta (aug-cc-pVQZ) basis set of Woon and Dunning for all atoms,[19] supplemented with an additional set of bond functions (3*s*3*p*2*d*1*f*1*g*) (where α = 0.9, 0.3, 0.1 for 3*s* and 3*p*; α = 0.6, 0.2 for 2*d*; α = 0.3 for *f* and *g*) placed at the mid-point of the intermolecular axis *R*.[20,21] The supermolecule approach was used to produce the intermolecular potential energy $\Delta V(R,\theta,Q_3)$, which is defined as the difference between the energy of the CO_2–He complex and the sum of the energies of the CO_2 and He monomers. The full counterpoise procedure[22] was employed to correct for basis set superposition error (BSSE). All calculations were carried out using the MOLPRO package.[23]

The calculations were performed on a regular grid for all three degrees of freedom. Five grid points corresponding to Q_3 = −0.115863, −0.054977, 0.0, 0.054977, and 0.115863 Å were chosen for the CO_2 stretching coordinate, while a relatively dense grid of 30 points ranging from 2.2 to 10.0 Å was used for the *R* stretching coordinate. The bending coordinate was also sampled by a fairly dense grid consisting of 23 angles, 19 distributed from 0 to 180° at intervals of 10°, plus four additional points (at 75, 85, 95 and 105°) in the region near the T-shaped minimum. This yielded a total of 2070 symmetry-unique points, a listing of which may be obtained from the authors or from the journal's on-line data archive.†

Our overall three-dimensional (3D) potential energy function for CO_2–He is then written as

$$V(R,\,\theta,\,Q_3) = V_{CO_2}(Q_3) + \Delta V(R,\,\theta,\,Q_3) \qquad (2)$$

where $V_{CO_2}(Q_3)$ is the effective one-dimensional (1D) potential energy curve for the asymmetric stretch of an isolated CO_2 molecule, and $\Delta V(R,\,\theta,\,Q_3)$ is the counterpoise-corrected interaction potential described above. The calculation of the 1D potentials governing the ν_3 vibration of the isolated CO_2 monomer were performed at the same [CCSD(T)]/aug-cc-pVQZ level described above. This strategy was used to construct recent *ab initio* 3D potential energy functions for CO_2–H_2 and N_2O–H_2,[24–26] and in earlier empirical treatments of H_2-{rare gas} complexes.[27–30] For a chosen fixed value of the average C–O bond length, the potential energy was computed at 29 values of Q_3 ranging from 0.0 to 0.5 Å, and those values were fitted to the even-power polynomial sexpansion:

$$V_{CO_2}(Q_3) = \sum_{n=0(2)} a_n (Q_3)^n \qquad (3)$$

The CO_2 monomer geometry, and hence also the effective 1D potential $V_{CO_2}(Q_3)$ and the intermolecular potential $\Delta V(R,\,\theta,\,Q_3)$, depend not only on Q_3, but also on the an assumed fixed value for the symmetric stretch coordinate $Q_1 = \{r_{CO_{[1]}} + r_{CO_{[2]}}\}/\sqrt{2}$. The average values of the C–O bond length in the ground (v_3 = 0) and first excited (v_3 = 1) states of CO_2 are r_0 = 1.162086 and 1.166695 Å, respectively.[17] These values were used to define the fixed values of Q_1, denoted $\bar{Q}_1^{[v_3]}$, governing the CO_2 geometry when generating the effective 1D potentials $V_{CO_2}(Q_3) = V_{CO_2}^{\bar{Q}_1[v_3]}(Q_3)$ used to define the total potential function of eqn (2) in the 3D eigenvalue calculations. This approach differs from that used in recent 3D treatments of CO_2–H_2 and N_2O–H_2, in which the same fixed Q_1 value was used to define the effective 1D monomer stretching potentials when treating states of the complex associated with both the ground (v_3 = 0) and first excited (v_3 = 1) levels of the chromophore.[25,26]

An ideal effective 3D treatment would be to generate the entire grid of $\Delta V(R,\,\theta,\,Q_3)$ values with the CO_2 geometry constrained, in turn, by the $\bar{Q}_1^{[v_3]}$ value for each monomer vibrational level (v_3) of interest. However, this would be computationally expensive, and we believe (and the tests in section IV confirm) that the main effect of the v_3-dependence of $\bar{Q}_1^{[v_3]}$ is captured by its effect on the effective 1D monomer potential $V_{CO_2}^{\bar{Q}_1[v_3]}(Q_3)$. Hence, our overall potential $V(R,\,\theta,\,Q_3)$ for complexes formed from CO_2 in its ground (v_3 = 0) and first excited (v_3 = 1) states was generated by using a common $\Delta V(R,\,\theta,\,Q_3)$ function defined by $\bar{Q}_1^{[v_3=0]}$, but with $V_{CO_2}(Q_3)$ calculated using the different effective 1D potentials $V_{CO_2}^{\bar{Q}_1[v_3]}(Q_3)$ for v_3 = 0 and 1. The coefficients of the polynomial expansions used to represent the 1D effective CO_2 asymmetric stretch potentials of eqn (3) are presented in Table 1.

B Hamiltonian without separating the intra- and intermolecular vibrations

Within the Born–Oppenheimer approximation, the ro-vibrational Hamiltonian of the CO_2–He complex in the Jacobi coordinate system (R, θ, Q_3) with the total angular momentum represented in the body-fixed reference frame can be written as[31–33]

$$\begin{aligned}\hat{H} = &-\frac{\hbar^2}{2\mu}\frac{\partial^2}{\partial R^2} - \frac{\hbar^2}{2M}\frac{\partial^2}{\partial {Q_3}^2} \\ &+ \left(\frac{\hbar^2}{2\mu R^2} + \frac{\hbar^2}{2I}\right)\left(\frac{-1}{\sin\theta}\frac{\partial}{\partial\theta}\sin\theta\frac{\partial}{\partial\theta} + \frac{\hat{J}_z^2}{\sin^2\theta}\right) \\ &+ \frac{\hat{J}^2 - 2\hat{J}_z^2}{2\mu R^2} + \frac{\cot\theta}{2\mu R^2}[(\hat{J}_x + i\hat{J}_y) + (\hat{J}_x - i\hat{J}_y)]\hat{J}_z \\ &+ \frac{\hbar}{2\mu R^2}\frac{\partial}{\partial\theta}[(\hat{J}_x + i\hat{J}_y) - (\hat{J}_x - i\hat{J}_y)] + V(R,\theta,Q_3)\end{aligned} \qquad (4)$$

in which $\mu^{-1} = {m_{He}}^{-1} + (2m_O + m_C)^{-1}$ and $M = m_C m_O/(2m_O + m_C)$, where m_{He}, m_C and m_O are the masses of the He, C and O atoms,[34] respectively, I is the rotational moment of

Table 1 Expansion coefficients a_n[$cm^{-1}/Å^n$] of the one-dimensional potentials $V_{CO_2}^{\bar{Q}_1[v3]}(Q3)$ of eqn (3) for v_3 = 0 and v_3 = 1

Parameters	(v_3 = 0)	(v_3 = 1)
a_0	0.0	0.0
a_2	372070.1	359320.9
a_4	648373.0	630396.0
a_6	486800.0	473200.0
a_8	159000.0	155000.0

inertia of CO_2, and $V(R, \theta, Q_3)$ is the total potential energy of the system. The operators $\hat{J}_x$, $\hat{J}_y$ and $\hat{J}_z$ are the components of the total angular momentum operator $\hat{J}$ in the body-fixed frame, and the z axis of the body-fixed frame lies along the Jacobi radial vector R. The above Hamiltonian contains full vibration–rotation coupling.

A direct-product discrete variable representation (DVR) grid was used in the ro-vibrational level energy calculation for the CO_2–He complex.[35] An 80-point sin-DVR grid extending to 10 Å was used for the radial R stretching coordinate, and a 70-point Gauss–Legendre grid used for angular variable. For the Q_3 coordinate, tests showed that five potential-optimized DVR grid points for the asymmetric stretch vibration of the CO_2 molecule sufficed to represent properly the upper and lower levels of the fundamental ν_3 vibration of CO_2. The Lanczos algorithm was used to calculate the ro-vibrational energy levels by recursively diagonalizing the discretized Hamiltonian matrix.[36] Tests showed that doubling the density of DVR points affected the calculated level energies by less than 0.00001 cm^{-1}, while extending the outer end of the radial grid from 10 to 15 Å affected predicted spectroscopic transition energies by less than 0.0001 cm^{-1} and level energies by less than 0.00075 cm^{-1}.

Since the effective 1D potentials $V_{CO_2}^{\bar{Q}_1[v_3]}(Q_3)$ do not take full account of coupling to the other internal degrees of freedom of CO_2, absolute IR transition energies calculated from our 3D surfaces cannot be expected to be particularly accurate. Thus, the calculated binding energies for complexes formed from $v_3 = 0$ and 1 CO_2 should be combined with the experimental CO_2 vibrational level spacings when generating predicted IR transition energies.

C Hamiltonian with separation of the intra- and intermolecular vibrations

The above approach incorporates full coupling between the intermolecular and Q_3 vibrations. However, convergence of the eigenvalue calculations is very slow at the high internal energies associated with excitation of the ν_3 vibration of CO_2, since it requires a relatively large number of Lanczos iterations. It would therefore be highly desirable to separate the treatment of the inter- and intramolecular motions. Since the ν_3 vibrational mode of CO_2 has a much higher frequency than do the intermolecular modes, Born–Oppenheimer separation type arguments suggest that it should be a good approximation to introduce such a separation, as long as the off-diagonal vibrational coupling is sufficiently small. In this approximation, the total vibrational wave function would be written as the direct product

$$\Psi_v(R, \theta, Q_3) = \phi_v(R, \theta)\psi_v(Q_3) \quad (5)$$

where v is the quantum number for a specific vibrational state of the free CO_2 molecule, and the associated vibrational wavefunction $\psi_v(Q_3)$ is obtained by solving the 1D Schrödinger equation:

$$\left[\frac{-\hbar^2}{2M}\frac{d^2}{dQ_3^2} + V_{CO_2}^{\bar{Q}_1^{[v_3]}}(Q_3)\right]\psi_v(Q_3) = E_v\psi_v(Q_3) \quad (6)$$

The present work focuses on complexes formed from CO_2 in the ground ($v_3 = 0$) and first excited ($v_3 = 1$) states of its asymmetric stretch ν_3 vibration. Using eqn (5), the vibrationally averaged CO_2–He interaction potential for CO_2 in vibrational level v_3 is

$$\overline{V}_{[v_3]}(R, \theta) = \int_{-\infty}^{\infty} \psi_{v_3}^*(Q_3)\Delta V(R, \theta, Q_3)\psi_{v_3}(Q_3)dQ_3 \quad (7)$$

and the associated two-dimensional intermolecular Hamiltonian is

$$\hat{H} = -\frac{\hbar^2}{2\mu}\frac{\partial^2}{\partial R^2} + \frac{\hat{l}^2}{2\mu R^2} + B_v\hat{j}^2 + \overline{V}_{[v_3]}(R, \theta) \quad (8)$$

in which $\hat{j}$ the total angular momentum operator for CO_2, $\hat{l}$ is the angular momentum operator associated with rotation of the axis R, and

$$B_v = \left\langle \psi_v \left| \frac{\hbar^2}{2I(Q_3)} \right| \psi_v \right\rangle \quad (9)$$

is the CO_2 inertial rotational constant, where $I(Q_3)$ is the instantaneous CO_2 moment of inertia. Note that the differences between the vibrationally averaged intermolecular potentials $\bar{V}_{[v_3]}$ for different values of v_3 arise both because the wavefunctions $\psi_{v_3}(Q_3)$ are associated with different values of v_3, and because they were obtained from different effective 1D potentials $V_{CO_2}^{\bar{Q}_1[v_3]}(Q_3)$.

Using the above approach to average the 3D intermolecular interaction potential $\Delta V(R, \theta, Q_3)$ yielded separate two-dimensional (2D) potentials for $v_3 = 0$ and 1. Those vibrationally averaged potentials $\bar{V}_{[v_3]}(R,\theta)$ are used in the simulations of spectroscopic data described in section IV, and should be useful for simulations of larger CO_2–$(He)_N$ clusters. The 2D eigenvalue calculations reported below utilized the experimental CO_2 rotational constants $B_{v_3}^{obs} = 0.390219$ and 0.387141 cm^{-1} for $v_3 = 0$ and 1, respectively, in eqn (8). However, almost exactly the same results are obtained using B_v values generated from eqn (9) if the 1D potential functions used in eqn (6) when determining the wavefunctions $\psi_{v_3}(Q_3)$ are the $V_{CO_2}^{\bar{Q}_1[v_3]}(Q_3)$ functions discussed above.

III. Analytic potential energy surface for CO_2–He

A Three-dimensional potential energy function

Our *ab initio* intermolecular potential energies $\Delta V(R, \theta, Q_3)$ for the CO_2–He system were fitted to a generalization of the MLR potential function form,[15,16] which is written as:

$$\Delta V_{MLR}(R, \theta, Q_3) = \mathscr{D}_e(\theta, Q_3)\times \left[1 - \frac{u_{LR}(R, \theta, Q_3)}{u_{LR}(R_e, \theta, Q_3)}e^{-\beta(R,\theta,Q_3)\cdot y_p(R,\theta,Q_3)}\right]^2 \quad (10)$$

in which $\mathscr{D}_e(\theta, Q_3)$ is the depth and $R_e(\theta, Q_3)$ the position of the minimum along a radial cut through the potential at angle θ for a particular value of Q_3, while $u_{LR}(R, \theta, Q_3)$ is a function which defines the (attractive) limiting long-range behaviour of the effective 1D potential along that cut:

$$\Delta V(R, \theta, Q_3) \simeq \mathscr{D}_e(\theta, Q_3) - u_{LR}(R, \theta, Q_3) \quad (11)$$

Since both He and CO_2 are non-polar, the appropriate functional form for $u_{LR}(R, \theta, Q_3)$ is[37]

$$u_{LR}^{MLR}(R,\theta,Q_3) = \frac{C_6(\theta,Q_3)}{R^6} + \frac{C_8(\theta,Q_3)}{R^8} \quad (12)$$

and the denominator factor $u_{LR}(R_e, \theta, Q_3)$ is that same function evaluated at $R = R_e(\theta, Q_3)$. The radial behaviour of the exponent in eqn (10) is expressed using the dimensionless radial variable

$$y_p(R,\theta,Q_3) = \frac{R^p - R_e(\theta,Q_3)^p}{R^p + R_e(\theta,Q_3)^p} \quad (13)$$

where p is a small positive integer which must be greater than the difference between the largest and smallest (inverse) powers in eqn (12), $p > (8–6)$,[16] and the exponent coefficient function $\beta(R, \theta, Q_3)$ is a (fairly) slowly varying function of R, which we write as a constrained polynomial:

$$\beta(R,\theta,Q_3) = y_p(R,\theta,Q_3)\beta_\infty(\theta,Q_3) + [1 - y_p(R,\theta,Q_3)] \times \sum_{i=0}^{N} \beta_i(\theta,Q_3) y_p(R,\theta,Q_3)^i \quad (14)$$

Note that the definition of $y_p(R, \theta, Q_3)$ and the algebraic structure of eqns (10) and (14) mean that $\beta(R_e, \theta, Q_3) = \beta_0(\theta, Q_3)$, and that $\lim_{R\to\infty}\beta(R, \theta, Q_3) \equiv \beta_\infty(\theta, Q_3) = \ln\{2\mathscr{D}_e(\theta,Q_3)/u_{LR}(R_e,\theta,Q_3)\}$. The parameters $\mathscr{D}_e(\theta, Q_3)$, $R_e(\theta, Q_3)$, and the various $\beta_i(\theta, Q_3)$ all are expressed as polynomials expansions in Q_3 and Legendre expansions in θ, written in the form

$$A(\theta,Q_3) = \sum_{\lambda=0}\sum_{k=0} A^{\lambda k} Q_3^k P_\lambda(\cos\theta) \quad (15)$$

where $A = \mathscr{D}_e$, R_e or β_i.

Following Hutson *et al.*,[37] the leading Van der Waals coefficients $C_6(\theta, Q_3)$ are expanded as

$$C_6(\theta,Q_3) = \sum_{\lambda=0(2)}^{2} [C_{6,ind}^{\lambda}(Q_3) + C_{6,disp}^{\lambda}(Q_3)] P_\lambda(\cos\theta) \quad (16)$$

where the induction term is approximated as

$$C_{6,ind}^{\lambda}(Q_3) = [\mu_{CO_2}(Q_3)]^2 \alpha_{He} \quad (17)$$

in which $\mu_{CO_2}(Q_3)$ is the stretching-dependent CO_2 dipole moment and α_{He} the polarizability of atomic He. The equilibrium value of the isotropic dispersion coefficient $C_{6,disp}^0(Q_3 = 0)$ is calculated from the He and CO_2 pseudo-dipole oscillator strength distributions (pseudo-DOSDs) of Meath and coworkers,[38,39] and its Q_3 dependence is represented by that of the isotropic average polarizability of CO_2, $\bar{\alpha}(Q_3) = [\alpha_{||}(Q_3) + 2\alpha_\perp(Q_3)]/3$:

$$C_{6,disp}^0(Q_3) = C_{6,disp}^0(Q_3 = 0)\left\{\frac{\bar{\alpha}(Q_3)}{\bar{\alpha}(Q_3 = 0)}\right\} \quad (18)$$

The leading anisotropic dispersion coefficient $C_{6,disp}^2$ is then defined in terms of $C_{6,disp}^0(Q_3)$ and the Q_3-dependent parallel ($\alpha_{||}$) and perpendicular ($\alpha_\perp$) polarizabilities of CO_2:

$$C_{6,disp}^2(Q_3) = C_{6,disp}^0(Q_3)\left\{\frac{\alpha_{||}(Q_3) - \alpha_\perp(Q_3)}{\alpha_{||}(Q_3) + 2\alpha_\perp(Q_3)}\right\} \quad (19)$$

The Q_3-dependent functions representing $\mu_{CO_2}(Q_3)$, $\alpha_{||}(Q_3)$, and $\alpha_\perp(Q_3)$ appearing in the above expressions were all taken from the recent theoretical work of Haskopoulos and Maroulis.[40] Since we choose to represent our potential in "spectroscopists' units", cm^{-1} and Å, it is convenient to introduce a stretching coordinate in atomic units, $\Delta R = \sqrt{2}Q_3/a_0 = 2.672476Q_3$ (for Q_3 in Å), in terms of which our expression for the various dispersion coefficients may be written (in units [cm^{-1} $Å^6$]) as:

$$C_{6,ind}^0(Q_3) = C_{6,ind}^2(Q_3) = 6665.7414[-1.21(\Delta R) + 0.02(\Delta R)^2]^2 \quad (20)$$

$$C_{6,disp}^0(Q_3) = 72431.0\{1 + [0.34(\Delta R)^2 - 0.33(\Delta R)^4]/17.5372\} \quad (21)$$

$$C_{6,disp}^2(Q_3) = C_{6,disp}^0(Q_3)\left\{\frac{13.9222 - 2.93(\Delta R)^2 + 1.00(\Delta R)^4}{52.6116 + 1.02(\Delta R)^2 - 0.99(\Delta R)^4}\right\} \quad (22)$$

The coefficients $C_8^0(Q_3)$ and $C_8^2(Q_3)$ are then calculated from $C_6^0(Q_3) = [C_{6,disp}^0(Q_3) + C_{6,ind}^0(Q_3)]$ and the fixed values of the ratios $C_8^0/C_6^0 = 4.65$ $Å^2$ and $C_8^2/C_6^0 = 4.85$ $Å^2$ reported by Pack.[41]

B Least-squares fits

To commence any non-linear least-squares fit, it is necessary to have realistic initial trial values of the fitting parameters. In the present case of fits to the 3D Morse/Long-Range (3D-MLR) form of eqn (10), they were obtained in the following manner. First, a fit to the ordinary 1D MLR form (depending only on R) was performed for all 690 distinct combinations of θ and Q_3, using program phiFIT.[42] This involved some experimentation to ascertain the most appropriate choice for the integer parameter p appearing in the definition of the radial variable $y_p(R;\theta,Q_3)$ of eqn (13), and for the order N of the exponent polynomial of eqn (14). The resulting values of $\mathscr{D}_e(\theta,Q_3)$, $R_e(\theta,Q_3)$, and of $\beta_i(\theta,Q_3)$ (for $i = 0–N$) were then fitted to the (linear) Legendre expansions in θ and polynomials expansions in Q_3 of eqn (15), and the resulting expansion coefficients $\{A^{\lambda,k}\}$ used as starting parameters in the global 3D fit to eqn (10).

In the fits described below, the input *ab initio* energies were weighted by assigning them uncertainties of $u_i = 0.1$ cm^{-1} for the attractive region where $\Delta V(R,\theta,Q_3) \le 0.0$ cm^{-1}, and $u_i = \Delta V(R,\theta,Q_3) + 5.0]/50.0$ cm^{-1} for the repulsive region where ($\Delta V(R,\theta,\phi) > 0.0$ cm^{-1}). Using these weights, a fit with an RMS residual discrepancy of 0.032 cm^{-1} is obtained on fitting the 2832 *ab initio* points at energies $\Delta V(R,\theta,Q_3) < 1000$ cm^{-1} to a 3D-MLR potential defined by only 55 fitting parameters. At the resolution of Fig. 1, the resulting fitted potential clearly passes through all *ab initio* points for any given combination of θ and Q_3. The values of the resulting set of potential parameters are presented in Table 2, while a FORTRAN subroutine for generating this potential may be obtained from the authors or from the journal's

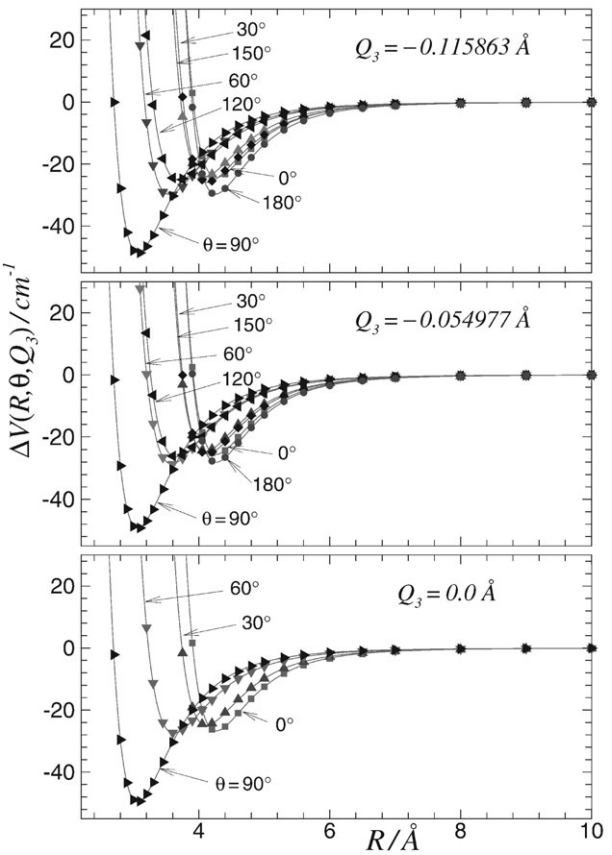

Fig. 1 *Ab initio* interaction energies and cuts through our analytic 3D potential energy surface for CO_2–He at various θ and Q_3 values.

supplementary data archive.† The compact form of the final parameters reflects the use of the sequential rounding and refitting procedure of ref. 43 in our fitting program.

C Vibrationally-averaged two-dimensional potential functions

For each of the 690 combinations of $\{R,\theta\}$ defining our grid of potential function values, eqn (7) was used to average our analytic 3D potential over the Q_3 coordinate to determine vibrationally averaged potential function values for the interaction of $CO_2(v_3 = 0)$ and $CO_2(v_3 = 1)$ with He. Similarly, vibrationally-averaged values of the long-range potential parameters $\bar{C}_6^0$ and $\bar{C}_6^2$ were obtained by vibrationally averaging the expressions given in eqns (20)–(22) using the 1D eigenfunctions $\psi_{v_3}(Q_3)$ of eqn (6), while the analogous $\bar{C}_8^{\lambda}$ coefficients were again fixed by ratios. With the angle-dependent dispersion coefficients defined in this manner, the two arrays of 690 vibrationally averaged potential energy values were then fitted to 2D versions of the generalized MLR function of eqns (10)–(14) in which the parameters $A(\theta,Q_3)$, for $A = \mathscr{D}_e$, R_e and β_i are replaced by $\bar{A}(\theta)$, and eqn (15) by

$$\bar{A}(\theta) = \sum_{\lambda} \bar{A}^{\lambda} P_{\lambda}(\cos\theta) \qquad (23)$$

Note that these $\bar{A}^{\lambda}$ values are determined by fitting to the vibrationally-averaged 2D potential function arrays, and not by vibrationally averaging the expressions for $A(\theta,Q_3)$ determined from the fit to the 3D potential function array. The parameters defining the resulting 2D potential energy surfaces for $^{12}C^{16}O_2(v_3 = 0)$ – He and $^{12}C^{16}O_2(v_3 = 1)$ – He are presented in Table 3. These 2D fits to interaction energies below 1000 cm^{-1} require only 24 free parameters, and yielded RMS discrepancies of $\sim$0.008 cm^{-1}.

Table 2 Expansion coefficients $\mathscr{D}_e^{\lambda,k}$ [cm^{-1}], $R_e^{\lambda,k}$ [Å] and $\beta_i^{\lambda,k}$ defining our original (unmorphed) analytic 3D-MLR potential energy surface for CO_2–He, with the long-range coefficients defined by eqns (20)–(22) and by the fixed ratios $C_8^0/C_6^0 = 4.65[Å^2]$ and $C_8^2/C_6^0 = 4.85[Å^2]$

$\mathscr{D}_e^{0,0}$	32.070	$R_e^{0,0}$	3.61855	$\beta_0^{0,0}$	0.0308
$\mathscr{D}_e^{0,2}$	2.8	$R_e^{0,2}$	0.146	$\beta_0^{1,1}$	−0.304
$\mathscr{D}_e^{1,1}$	−10.43	$R_e^{1,1}$	0.5637	$\beta_0^{2,0}$	0.9402
$\mathscr{D}_e^{2,0}$	−14.849	$R_e^{2,0}$	0.83738	$\beta_0^{3,1}$	0.11
$\mathscr{D}_e^{2,2}$	25.4	$R_e^{2,2}$	−0.489	$\beta_0^{4,0}$	−0.019
$\mathscr{D}_e^{3,1}$	49.45	$R_e^{3,1}$	−0.8476	$\beta_0^{0,0}$	0.71
$\mathscr{D}_e^{4,0}$	14.646	$R_e^{4,0}$	−0.2619	$\beta_1^{1,1}$	−0.74
$\mathscr{D}_e^{4,2}$	−33.0	$R_e^{4,2}$	0.21	$\beta_1^{2,0}$	0.253
$\mathscr{D}_e^{5,1}$	−31.47	$R_e^{5,1}$	0.2919	$\beta_2^{0,0}$	−0.237
$\mathscr{D}_e^{6,0}$	−8.086	$R_e^{6,0}$	0.09393	$\beta_2^{1,1}$	−0.40
$\mathscr{D}_e^{6,2}$	52.0	$R_e^{6,2}$	−0.20	$\beta_2^{2,0}$	−0.21
$\mathscr{D}_e^{7,1}$	23.7	$R_e^{7,1}$	−0.119	$\beta_3^{0,0}$	0.07
$\mathscr{D}_e^{8,0}$	4.332	$R_e^{8,0}$	−0.0312	$\beta_3^{1,1}$	−1.9
$\mathscr{D}_e^{8,2}$	−35.0	$R_e^{9,1}$	0.014	$\beta_3^{2,0}$	−0.29
$\mathscr{D}_e^{9,1}$	−13.5	$R_e^{10,0}$	0.0084		
$\mathscr{D}_e^{10,0}$	−2.15	$R_e^{11,1}$	0.009		
$\mathscr{D}_e^{10,2}$	27.0	$R_e^{12,0}$	−0.0015		
$\mathscr{D}_e^{11,1}$	7.3				
$\mathscr{D}_e^{12,0}$	0.98				
$\mathscr{D}_e^{12,2}$	−13				
$\mathscr{D}_e^{13,1}$	−3.8				
$\mathscr{D}_e^{14,0}$	−0.43				
$\mathscr{D}_e^{15,1}$	1.5				
$\mathscr{D}_e^{16,0}$	0.18				

Table 3 Expansion coefficients $\bar{\mathscr{D}}_e^{\lambda}$[$cm^{-1}$], $\bar{R}_e^{\lambda}$ [Å] and $\bar{\beta}_i^{\lambda}$ defining our unmorphed two-dimensional vibrationally averaged potential energy surfaces for $^{12}C^{16}O_2(v_3)$–He for $v_3 = 0$ and 1. The morphing would be incorporated by multiplying all of the $\bar{R}_e^{\lambda}$ values by the scaling factor $f_{R_e} = 0.99577$, and by multiplying the $\bar{\mathscr{D}}_e^{\lambda}$ factors for the $v_3 = 1$ surface by the factor $f_{D_e}^{[v_3=1]} = 0.99842$

Parameters defining 2D-MLR PES for $^{12}C^{16}O_2(v_3 = 0)$–He					
$\bar{\mathscr{D}}_e^0$	32.039	$\bar{R}_e^0$	3.61900	$\bar{\beta}_0^0$	0.0304
$\bar{\mathscr{D}}_e^2$	−14.787	$\bar{R}_e^2$	0.83644	$\bar{\beta}_0^2$	1.0010
$\bar{\mathscr{D}}_e^4$	14.616	$\bar{R}_e^4$	−0.26198	$\bar{\beta}_0^4$	−0.0172
$\bar{\mathscr{D}}_e^6$	−8.049	$\bar{R}_e^6$	0.09367	$\bar{\beta}_0^6$	0.6961
$\bar{\mathscr{D}}_e^8$	4.315	$\bar{R}_e^8$	−0.03118	$\bar{\beta}_1^0$	0.180
$\bar{\mathscr{D}}_e^{10}$	−2.135	$\bar{R}_e^{10}$	0.00830	$\bar{\beta}_2^0$	−0.235
$\bar{\mathscr{D}}_e^{12}$	0.975	$\bar{R}_e^{12}$	−0.00142	$\bar{\beta}_2^2$	−0.203
$\bar{\mathscr{D}}_e^{14}$	−0.439			$\bar{\beta}_3^0$	0.15
$\bar{\mathscr{D}}_e^{16}$	0.184				
$\bar{C}_6^0$	72457.62	$\bar{C}_8^0/\bar{C}_6^0$	4.65		
$\bar{C}_6^2$	19136.06	$\bar{C}_8^2/\bar{C}_6^0$	4.85		
Parameters defining 2D-MLR PES for $^{12}C^{16}O_2(v_3 = 1)$–He					
$\bar{\mathscr{D}}_e^0$	31.979	$\bar{R}_e^0$	3.62001	$\bar{\beta}_0^0$	0.0291
$\bar{\mathscr{D}}_e^2$	−14.637	$\bar{R}_e^2$	0.83496	$\bar{\beta}_0^2$	1.0003
$\bar{\mathscr{D}}_e^4$	14.559	$\bar{R}_e^4$	−0.26246	$\bar{\beta}_0^4$	−0.0161
$\bar{\mathscr{D}}_e^6$	−7.977	$\bar{R}_e^6$	0.09341	$\bar{\beta}_0^6$	0.691
$\bar{\mathscr{D}}_e^8$	4.281	$\bar{R}_e^8$	−0.03117	$\bar{\beta}_1^0$	0.177
$\bar{\mathscr{D}}_e^{10}$	−2.104	$\bar{R}_e^{10}$	0.00809	$\bar{\beta}_2^0$	−0.237
$\bar{\mathscr{D}}_e^{12}$	0.964	$\bar{R}_e^{12}$	−0.00125	$\bar{\beta}_2^2$	−0.204
$\bar{\mathscr{D}}_e^{14}$	−0.457			$\bar{\beta}_3^0$	0.15
$\bar{\mathscr{D}}_e^{16}$	0.193				
$\bar{C}_6^0$	72510.69	$\bar{C}_8^0/\bar{C}_6^0$	4.65		
$\bar{C}_6^2$	19063.06	$\bar{C}_8^2/\bar{C}_6^0$	4.85		

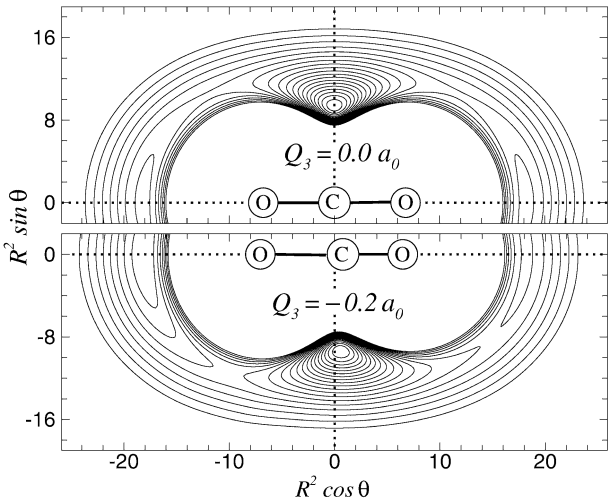

Fig. 2 Contour plots of our potential energy surface for CO_2–He in cylindrical coordinates for $Q_3 = 0.0a_0$ (upper) and $Q_3 = -0.2a_0$ (lower).

IV. Results and discussion

A Features of the three-dimensional potential energy surface

For $Q_3 = 0.0$ and -0.2 au, Fig. 2 displays contour plots of our fitted 3D potential energy surface for CO_2–He in the coordinate system $x = R^2\cos\theta$, $y = R^2\sin\theta$, where the radial factor R^2 was introduced in order to spread out the contours and better illustrate the nature and locations of the various minima and saddle points. The upper panel of Fig. 2 shows the potential surface for the symmetric CO_2 configuration, $Q_3 = 0$. It has the form of a conventional 2D potential surface with the two C–O bond lengths fixed at the average ground-state value. As the He atom moves around the rigid linear CO_2, an absolute minimum of -49.57 cm^{-1} occurs for the T-shaped geometries at $R = 3.061$ Å and $\theta = 90°$, and local minima of -26.69 cm^{-1} appear at the linear geometries where $R = 4.264$ Å and $\theta = 0$ or 180°. The other stationary points on this surface are the barriers with energy -24.41 cm^{-1} at $R = 3.977$ Å and $\theta = 90 \pm 49.2°$ on the minimum energy paths between the absolute and local minima. As shown by rows 3–6 of Table 4, the geometries and energies of these stationary points are in reasonable agreement with those associated with previous *ab initio* surfaces for this system.[4–6] However, rows 7 and 8 show that they differ substantially from those of two earlier empirical potentials which have no barrier along the minimum energy path between the linear and T-shaped geometries[2,3] (*cf.* Fig. 3).

The lower panel of Fig. 2 shows the potential energy surface for $Q_3 = -0.2\ a_0$; this amplitude is slightly outside the classical turning points at ± 0.107 and $\pm 0.185a_0$ and the root mean square amplitudes of $\bar{Q}_3^{\rm rms} = 0.075$ and $0.130a_0$ for $CO_2(v_3 = 0)$ and $CO_2(v_3 = 1)$, respectively. In this case the T-shaped minimum lies at almost the same radial distance, $R = 3.062$ Å, but its angular position shifts toward the compressed CO bond, to $\theta = 86.5°$, and the minimum becomes slightly deeper, at -49.79 cm^{-1}. Also, the two linear minima are no longer identical with regard to position ($R_e(\theta = 0°) = 4.269$ Å *vs.* $R_e(180°) = 4.251$ Å) or well depth

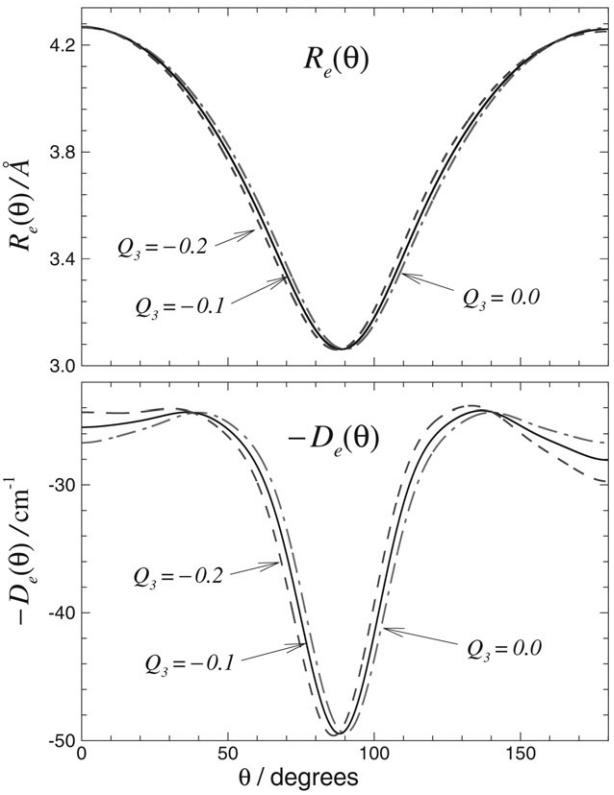

Fig. 3 Energy (b) and position (a) of the minima on cuts through our 3D potential energy surface for CO_2–He as functions of angle θ, for selected values of Q_3 (in atomic units a_0).

($\mathscr{D}_e(0°) = 24.58$ cm^{-1} *vs.* ($\mathscr{D}_e(180°) = 29.39$ cm^{-1}), the one associated with the compressed CO bond becoming shallower and the other one deeper. As shown in Fig. 2, the two transition states are also no longer identical. Parameters characterizing the various stationary point configurations are summarized in Table 4, while Fig. 3 shows how the positions $R_e(\theta,Q_3)$ and depths $\mathscr{D}_e(\theta,Q_3)$ of the radial minima depend on angle and Q_3.

B Bound states of our potential energy surface

The rovibrational energy levels of CO_2–He may be labeled by the six quantum numbers: v_3, n_s, n_b, J, K_a and K_c, where v_3 is the asymmetric stretch quantum number of CO_2, n_s and n_b are Van der Waals vibrational stretch and bending quantum numbers, and K_a and K_c denote the projections of the total angular momentum J onto the a and c principal axes of interia. Level energies and wave functions were obtained using the 3D DVR method and Lanczos propagation algorithm described in section II.B. While the 3D calculation are technically straightforward, the discussion of section II showed that the 1D potential $V_{CO_2}(Q_3) = V_{CO_2}^{\bar{Q}_1[v_3]}(Q_3)$ which we use to represent the internal vibrational motion of the free CO_2 molecule is different for the cases $v_3 = 0$ and 1, because of the different average C–O bond lengths for those states. This affects the 'pure 3D' calculations because it leads to slightly different 1D curves being included in the total potential energy $V(R,\theta,Q_3)$ (see eqn (2)) appearing in the 3D Hamiltonian of eqn (4).

Table 4 Properties of stationary points of the present (un-morphed) CO_2–He potential energy surface for representative values of the asymmetric stretch coordinate Q_3, and comparisons with results for previously reported surfaces. All entries are given as $\{R$ [Å], θ°, ΔV [cm^{-1}]$\}$, where $\theta = 0$ corresponds to the He atom lying at the end of the compressed CO bond

$Q_3(a_0)$	T-shaped minimum	Saddle point	Linear minimum	Type	Ref.
−0.2	{3.062, 86.5, −49.79}	{3.895, 131.0, −24.00}	{4.251, 180, −29.39}	Theory	Present
−0.2	{3.062, 86.5, −49.79}	{4.104, 28.7, −24.18}	{4.269, 0, −24.58}	Theory	Present
0.0	{3.061, 90.0, −49.57}	{3.977, 40.8, −24.41}	{4.264, 0, −26.69}	Theory	Present
0.0	{3.07, 90.0, −50.38}	{≈4.0, ≈40, ≈−30}	{4.25, 0, −28.94}	Theory	[6]
0.0	{3.1, 90.0, −45.98}	{3.95, 45, −23.57}	{4.3, 0, −26.31}	Theory	[5]
0.0	{3.103, 90.0, −44.41}	{4.104, 39, −24.60}	{4.26, 0, −27.69}	Theory	[4]
0.0	{3.14, 90.0, −41.00}	{*no saddle point*}	{4.75, 0, −15.80}	Empirical	[3]
0.0	{3.43, 90.0, −34.6}	{*no saddle point*}	{4.73, 0, −13.34}	Empirical	[2]

Column 2 of Table 5 lists the energies of the $J = 0$ vibrational levels of $CO_2(v_3 = 0)$–He and $CO_2(v_3 = 1)$–He on our 3D surface, and compares them to published results reported for some previously reported surfaces (columns 5–7).[3,4,6] Our surface supports five bound vibrational levels for complexes formed from either ground-state ($v_3 = 0$) or excited ($v_3 = 1$) CO_2, and the level energies for those two cases are very similar to one another. The nodal structure of the wavefunctions for these states, shown in Fig. 4, indicates that the first excited level is a vibrational bending state with quantum state labels $n_s = 0$ and $n_b = 1$, while the three higher ones are Van der Waals stretching states with labels $n_s = 1$ and $n_b = 0$, 1 and 2. Note, however, that while these $\{n_s,n_b\}$ 'assignments' are useful descriptive labels, they have no rigorous quantum mechanical significance.

The calculations described above were performed without invoking a separation of the intra- and intermolecular vibrational motions. However, since the internal energy of complexes formed from vibrationally excited $CO_2(v_3 = 1)$ is relatively high, many Lanczos steps are needed to fully converge the calculation of their eigenvalues. In particular, even for $J = 0$, about 35 000 Lanczos steps are required to obtain converged eigenvalues for all bound states of $CO_2(v_3 = 1)$–He, and many more steps are required for higher angular momentum states. In contrast, upon separation of intra- and intermolecular vibrations, only 1000 Lanczos steps are required to fully converge the bound state energies for CO_2 in either the ground ($v_3 = 0$) or excited ($v_3 = 1$) state. It is therefore important to ascertain the accuracy of results obtained by first averaging over the CO_2 stretching motion to obtain separate 2D potential energy surfaces associated with $v_3 = 0$ and 1, as described in section II.C.

Column 3 of Table 5 lists the vibrational energies calculated from the 2D vibrationally averaged potential energy surfaces associated with the ground ($v_3 = 0$) and first excited ($v_3 = 1$) states of CO_2, while column 4 shows their differences with the 3D results. The size of these differences clearly indicates that our vibrationally averaged 2D potentials provide a very reliable description of this system. An important contribution both to this good agreement and to the agreement with experiment described below is the use of different effective 1D potentials $V_{CO_2}^{\bar{Q}_1[v_3]}(Q_3)$ for different values of v_3. One indication of the fact that this is a good physical approximation is the fact that the value of $B_{v_3=1}$ for CO_2 calculated from eqn (9) differs from experiment by only 0.048% if the 1D wavefunction was obtained by solving eqn (6) for the potential $V_{CO_2}^{\bar{Q}_1[v_3=1]}(Q_3)$, while that difference increases by an order of magnitude (to 0.75%) if the 1D potential associated with $\bar{Q}_1^{[v_3=0]}$ is used. Moreover, use of $V_{CO_2}^{\bar{Q}_1[v_3=0]}(Q_3)$ in eqn (2) when generating the 3D vibrational energies of the complex for $v_3 = 1$ would increase the discrepancies shown in the bottom half of the fourth column of Table 5 by an order of magnitude.

A more subtle effect on the calculation is associated with the definition of the 1D function $\psi_{v_3=1}(Q_3)$ used to perform the vibrational averaging of eqn (7) for $v_3 = 1$. However, if that function is obtained from eqn (6) using the 1D potential obtained with $Q_1 = \bar{Q}_1^{[v_3=0]}$ rather than $Q_1 = \bar{Q}_1^{[v_3=1]}$, the discrepancies for the case $v_3 = 1$ seen in column 4 of Table 5 change very little.

Table 5 Energies (in cm^{-1}) for the five vibrational levels of our 3D-MLR potential energy surface for CO_2–He surface (expressed relative to the relevant asymptote), compared with published results for some previously reported surfaces

	Present work					
(n_s, n_b)	3D	2D	{3D − 2D}	Ref. 4	Ref. 3	Ref. 6
Complex formed from $CO_2(v_3 = 0)$						
(0, 0)	−17.041	−17.040	−0.001	−15.806	−15.689	−18.052
(0, 1)	−8.752	−8.751	−0.001	−7.143	−9.756	−9.247
(1, 0)	−7.644	−7.644	−0.000	−5.771	−6.968	−8.154
(1, 1)	−4.034	−4.032	−0.002	−3.035		
(1, 2)	−1.283	−1.283	0.000	−0.576		
Complex formed from $CO_2(v_3 = 1)$						
(0, 0)	−16.977	−16.975	−0.002	−15.818		
(0, 1)	−8.765	−8.762	−0.003	−7.155		
(1, 0)	−7.668	−7.666	−0.002	−5.781		
(1, 1)	−4.070	−4.065	−0.005	−3.068		
(1, 2)	−1.306	−1.303	−0.003	−0.596		

C Comparisons with experiment, and morphing the surface

A small number of high resolution measurements of pure rotational transitions of CO_2–He complexes have been reported by Xu and Jäger.[44] Table 6 compares their observed transition wavenumbers for the symmetric isotopologues (column 3) with those calculated from our vibrationally averaged 2D potential energy surface (columns 4 and 5). The fact, that the calculated values in column 4 are all approximately 0.58% smaller than experiment indicates that the moment of inertia of the complex implied by our pure *ab initio* surface is slightly too large. This property depends mainly on the average intermolecular bond length R_e, which is a natural parameter

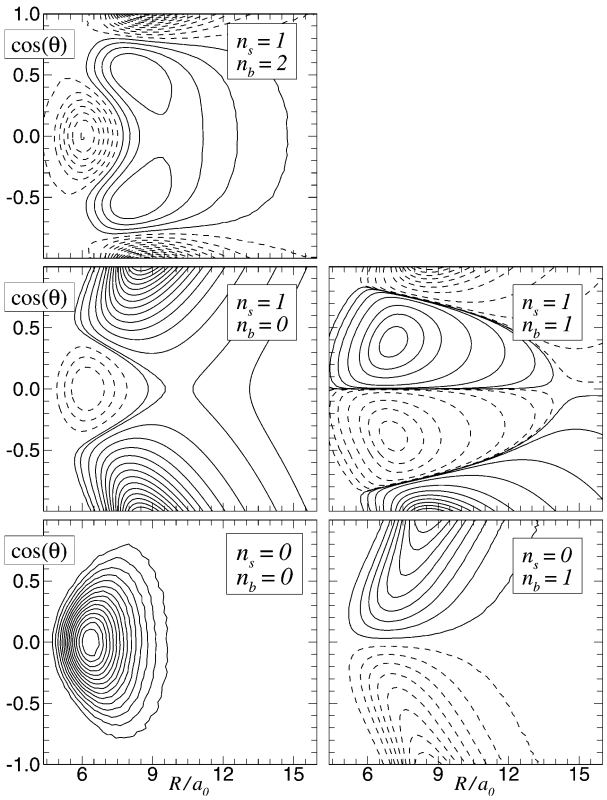

Fig. 4 Wave functions for the five lowest vibrational states of CO_2–He ($v_3 = 0$).

of the analytic MLR potential function form of eqn (10). It therefore seems appropriate to morph our potential energy surfaces by multiplying all of the $R_e^{\lambda k}$ expansion parameters of Table II and $\bar{R}_e^{\lambda}$ parameters of Table 3 by a common scaling factor in order to optimize the agreement with experiment. A non-linear least-squares optimization yielded the scaling factor $f_{R_e} = 0.99577$. While this factor differs somewhat from the value $\sqrt{0.9942} = 0.997$ implied by the results in column 5 of Table 6, that difference is readily explained by the fact that the zero-point energy of the system is 2/3 of the well depth, so the ground-state moment of inertia is not expected to scale simply as the square of R_e. In any case, the net result of this morphing (see columns 6 and 7 of Table 6) is that the RMS discrepancy with these experimental microwave data is reduced by two orders of magnitude.

Although there exist very few pure rotational data for CO_2–He,[44] sixty-six infrared transitions associated with excitation of the v_3 asymmetric stretch of the CO_2 monomer within the complex were reported by Weida *et al.*,[14] and forty-nine of them were assigned. Consideration of all pairs of such transition with a common upper or common lower level allows us to generate a wide range of experimental "pseudo" microwave data which may be used to further test our potential energy surfaces. The results of these tests are summarized in Table 7. Again, the predictions generated from our pure *ab initio* potential energy surface are already in quite good agreement with experiment. That agreement is substantially improved for our radially morphed 2D-MLR potentials, with the final level of agreement being close to the RMS experimental data uncertainty of ± 0.0019 cm^{-1}. Full listings of the individual differences summarized by Table 7 are available in Tables A-1 and A-2 of the supplementary data associated with this paper.†

Table 7 Comparison of experiment with pure rotational level spacings of $^{12}C^{16}O_2(v_3)$–He calculated from our vibrationally averaged 2D-PES, in which the experimental values are differences between observed infrared transitions[14] with a common upper state, for $v_3 = 0$, or a common lower state, for $v_3 = 1$

	Original 2D PESs		Re-morphed PESs	
	$v_3 = 0$	$v_3 = 1$	$v_3 = 0$	$v_3 = 1$
No. data	29	22	29	22
Range $\{J_{K_aK_c}\}$	$0_{00} - 6_{25}$	$1_{10} - 6_{16}$	$0_{00} - 6_{25}$	$1_{10} - 6_{16}$
Average{calc.–obs}	−0.0072	−0.0061	−0.0011	0.0003
RMSD{calc.–obs.}	0.0123	0.0092	−0.0022	0.0028

In order to simulate the absolute infrared transition energies for comparison with experiment, the difference between the binding energies on our vibrationally averaged 2D potential energy surfaces for $v_3 = 1$ and 0 is added to the experimental value of the fundamental band origin for the ν_3 transition CO_2, 2349.1433 cm^{-1}.[17] Table 8 summarizes comparisons with experiment of infrared transition energies calculated using our vibrationally averaged 2D-MLR potential energy surfaces for $v_3 = 0$ and 1, first without and then with the application of morphing parameters. Column 2 summarizes the differences with the $^{12}C^{16}O_2$–He data of Weida *et al.*[14] yielded by our unmorphed *ab initio* surfaces, while column 3 shows that application of only the f_{R_e} morphing factor only improves this agreement slightly. However, for both of these cases, the fact that the average deviation and RMS deviation have approximately the same magnitude indicates that most of the discrepancy is systematic. Moreover, the negative sign of the arithmetic average discrepancy indicates that the levels of our upper-state $CO_2(v_3 = 1)$–He potential surface are (relatively) somewhat too strongly bound. Thus, although the existing

Table 6 Comparison of experiment[44] with calculated pure rotational transition energies of CO_2–He isotopologues (in cm^{-1}) obtained from both our original (columns 4 & 5) and our radially morphed (columns 5 & 6) 2D potential energy surfaces

			Original PES		R_e–morphed PES	
Transition $J'_{K'_aK'_c}$–$J''_{K''_aK''_c}$	Isotopologue	Observed[44]	calc.	(calc./obs.)	calc.	(calc./obs.)
1_{01}–0_{00}	$^{16}O^{12}C^{16}O$–He	0.591577	0.588126	0.994166	0.591546	0.999946
1_{11}–0_{00}	$^{18}O^{12}C^{18}O$–He	0.578736	0.575424	0.994278	0.578759	1.000041
1_{01}–0_{00}	$^{16}O^{13}C^{16}O$–He	0.590824	0.587316	0.994063	0.590732	0.999844
1_{11}–0_{00}	$^{18}O^{13}C^{18}O$–He	0.578127	0.574756	0.994169	0.578088	0.999933
RMSD {calc.–obs.}:			0.003411		0.000054	

Table 8 Comparison of experiment with calculated infrared transition frequencies (in cm^{-1}) for the three symmetric isotopologues of CO_2–He

Potential:	Original	R_e morphed	R_e and $\mathscr{D}_e$ morphed		
Isotopologue	$^{12}C^{16}O_2$	$^{12}C^{16}O_2$	$^{12}C^{16}O_2$	$^{13}C^{16}O_2$	$^{12}C^{18}O_2$
Number of data	49	49	49	24	29
Mean{calc.–obs.}	−0.0435	−0.0407	−0.0003	0.0003	−0.0011
RMS{calc.–obs.}	0.0445	0.0424	0.0038	0.0020	0.0027
$\Delta\nu_0$ {band origin shift}	0.0647	0.0644	0.1088	0.1065	0.1083
$\delta(\Delta\nu_0)$ {calc.–obs.}	−0.0299	−0.0302	0.0142	0.0136	−0.0040

experimental data provide no information about the absolute well depths on either 2D surface, it does tell us that relative to that for $CO_2(v_3 = 0)$–He, the $CO_2(v_3 = 1)$–He surface is slightly too deep.

These observations led us to introduce a second morphing parameter to scale all of the $\bar{\mathscr{D}}_e^{\lambda}$ parameters defining our 2D-MLR potential for $CO_2(v_3 = 1)$–He. Applying a least-squares optimization procedure to the 49 assigned transitions for $^{12}C^{16}O_2$–He yielded the dimensionless morphing parameter $f_{\mathscr{D}e}^{[v_3=1]} = 0.99842$. Applying this scaling factor to the $\bar{\mathscr{D}}_e^{\lambda}$ vales for the $v_3 = 1$ surface yields the much improved level of agreement summarized by the fourth column of Table 8; it is gratifying to see that the remaining RMS discrepancy of 0.0038 cm^{-1} approaches the RMS experimental uncertainty of 0.0019 cm^{-1}.[14] The last two columns of Table 8 then show that this two-parameter morphing of our surfaces (by both $f_{R_e \text{ and } f\mathscr{D}e}^{[v_3=1]}$) yields similarly excellent agreement with McKellar's very recent IR data for the minor isotopologues $^{13}C^{16}O_2$–He and $^{12}C^{18}O_2$–He,[45] Tables A-3 and A-4 of the supplementary data provide detailed listings of the transitions used in these comparisons, while Tables A-5 to A-7† list the parameters $\bar{A}^{\lambda}$ of the associated vibrationally average 2D-MLR potentials for $^{13}C^{16}O_2$–He, $^{12}C^{18}O_2$–He, and $^{13}C^{18}O_2$–He.

V. Discussion and conclusions

This paper presents an accurate new analytic 3D potential energy surface for the CO_2–He complex which explicitly incorporates the dependence of the interaction energy on the Q_3 normal-mode coordinate of CO_2. This surface is based on *ab initio* interaction energies obtained at the CCSD(T) level with a large aug-cc-pVQZ basis set and with bond functions placed at the mid-point on the intermolecular axis. These *ab initio* results are fitted to a 3D generalization of the Morse/Long-Range (MLR) potential form which incorporates the correct theoretically known long-range inverse-power behaviour;[15,16] having this correct long-range behaviour is important if this potential is to provide a good description of a CO_2 molecule in medium to large sized $(He)_N$ clusters. The global 3D fit to the 2832 *ab initio* interaction energies below 1000 cm^{-1} had a root-mean-square residual of only 0.032 cm^{-1} and required only 55 fitting parameters. Analogous accurate 2D-MLR potential energy surfaces for CO_2–He complexes formed from CO_2 in its ground ($v_3 = 0$) and first excited ($v_3 = 1$) states were obtained by averaging this 3D surface over the Q_3 asymmetric stretch vibrational motion of CO_2, and tests showed that the approximate separation of variables to yield these 2D surfaces had no significant effect on the calculated eigenvalues.

The calculated spectroscopic properties of our pure *ab initio* potentials are in excellent agreement with experiment. In particular, for 29 rotational level spacings of $^{12}C^{16}O_2(v_3 = 0)$–He and 22 for $^{12}C^{16}O_2(v_3 = 1)$–He, the RMS discrepancies are 0.0123 and 0.0092 cm^{-1}, respectively, and a one-parameter morphing of our surfaces reduced these discrepancies by almost a factor of five. Similarly, for 49 infrared transitions of $^{12}C^{16}O_2$–He, the RMS discrepancy yielded by the fitted *ab initio* surfaces was 0.044 cm^{-1}, and introduction of a second morphing parameter reduced this discrepancy by an order of magnitude.

All previous potential energy surfaces for this system were two-dimensional, ignoring the effect of the Q_3 stretching coordinate of CO_2. However, their comparisons with the IR data for $^{12}C^{16}O_2$–He empirically corrected for the vibrational frequency shift by combining the calculated upper- and lower-level binding energies with the experimental band origin for the complex, rather than with the pure CO_2 vibrational energy. For the best of those earlier surfaces, the quality of agreement obtained in that way (RMS deviations of 0.0394 and 0.0222 cm^{-1} for the surfaces of ref. 4 and 6, respectively) were comparable to the result obtained here (0.0445 cm^{-1}, see Table 8) on combining the binding energies of our 2D pure (un-morphed) *ab initio* surfaces with the pure CO_2 vibrational energy. The level of agreement achieved here after our two-parameter morphing of our surfaces is an order of magnitude better than that. Thus, our final morphed potential energy surfaces (see Table 3) should provide an excellent foundation for simulations to predict the properties of CO_2 clustered with multiple He atoms.

As in all previously reported studies of the Van der Waals interactions of linear triatomic molecules, the present work assumes perfect adiabatic separability of the bending and symmetric-stretch modes of the linear molecule from all the other degrees of freedom. Since all existing data involve CO_2 in its $v_1 = v_2 = 0$ ground states, this implies that those degrees of freedom may be ignored. Our justification for this approximation is the fact that in a free CO_2 molecule, the leading potential energy coefficient due to inter-mode coupling is two orders of magnitude smaller than the harmonic force constant for the Q_3 vibration.[53] Since the total shift of the CO_2 ν_3 band origin due to binding with a He atom is only *ca.* 0.1 cm^{-1}, a correction to a 1% contribution to the vibrational fundamental due to inter-mode coupling would be very small. The good agreement with experiment for the pure rotational level spacings of our un-morphed potential energy surface attests to the validity of this approximation, at least as far as the spectroscopic properties of the perturbed ν_3 band are concerned.

In recent years it has become common to represent atom–molecule and molecule–molecule Van der Waals interaction potentials by generalizations of the 1D 'HFD'-type potentials initially devised by Scoles, Meath, Toennies and co-workers,[46–52] in which the potential is represented by a sum of a repulsive exponential term with attractive inverse-power dispersion (and induction) terms which are 'damped' to take account of charge overlap. In the generalization to atom–molecule and molecule–molecule systems, the parameters of these 1D forms

are generally simply expanded either in Legendre polynomials, or in terms of combinations of Legendre functions and powers of R.[5,6,30,54–56] However, the resulting fitted potential parameters have little direct physical significance or relationship to features of the surface. In contrast, the central parameters of the MLR form, $\mathscr{D}_e(\theta,Q_3)$ and $R_e(\theta,Q_e)$ directly characterize the position and depth of the potential minimum and its dependence on monomer orientation and internal stretching. Moreover, the leading terms in the limiting long-range tail of the potential are incorporated into the potential in a unified manner, rather than being an additive term which must be cut off to prevent unphysical behaviour at short distances. The MLR form also can equally readily be used for chemically bound species (such as[15,16,57] N_2, Ca_2 and MgH), in which the inverse-power dispersion terms contribute only a (very) small part of the binding energy. The relatively modest numbers of parameters required to yield an accurate fit to our *ab initio* points, and the very good agreement with experiment achieved with even the un-morphed surface attest to the efficacy of this representation.

One further advantage of the MLR form is that it is relatively straightforward to morph a global *ab initio* surface fitted in this way, simply by multiplying the expressions for $\mathscr{D}_e(\theta,Q_3)$ and $R_e(\theta,Q_e)$ (see eqn (15)) by scaling factors or functions. This allows one to use comparisons with experimental data to improve an *ab initio* surface without prejudicing its essentially correct subtle features of shape. In the present work, that morphing was done using simple constant scaling factors, but it could equally involve factors depending on monomer relative orientation or internal stretching, or even on the radial separation R, preferably expressed as functions of a dimensionless radial variable such as $y_p(R)$ (see eqn (13)), without doing violence to the nature of the overall representation. Thus, in addition to providing a very good description of the CO_2–He system, the present work introduces a very promising new approach for providing accurate and (relatively) compact representations of multi-dimensional potential energy surfaces.

References

1. G. A. Parker, R. L. Snow and R. T. Pack, *J. Chem. Phys.*, 1976, **64**, 1668.
2. M. Keil and G. A. Parker, *J. Chem. Phys.*, 1985, **82**, 1947.
3. L. Beneventi, P. Casavecchia, F. Vecchiocattivi, G. G. Volpi, U. Buck, Ch. Lauenstein and R. Schinke, *J. Chem. Phys.*, 1988, **89**, 4671.
4. G. Yan, M. H. Yang and D. Xie, *J. Chem. Phys.*, 1998, **109**, 10284.
5. F. Negri, F. Ancilotto, G. Mistura and F. Toigo, *J. Chem. Phys.*, 1999, **111**, 6439.
6. T. Korona, R. Moszynski, F. Thibault, J.-M. Launay, B. Bussery-Honvault, J. Boissoles and P. E. S. Wormer, *J. Chem. Phys.*, 2001, **115**, 3074.
7. K. Nauta and R. E. Miller, *J. Chem. Phys.*, 2001, **115**, 10254.
8. J. Tang, A. R. W. McKellar, F. Mezzacapo and S. Moroni, *Phys. Rev. Lett.*, 2004, **92**, 145503.
9. J. Tang and A. R. W. McKellar, *J. Chem. Phys.*, 2004, **121**, 181.
10. F. Paesani, Y. Kwon and K. B. Whaley, *Phys. Rev. Lett.*, 2005, **94**, 153401.
11. H. Hoshina, J. Lucrezi, M. N. Splipchenko, K. E. Kuyanov and A. F. Vilesov, *Phys. Rev. Lett.*, 2005, **94**, 195301.
12. R. Lehnig and W. Jäger, *Chem. Phys. Lett.*, 2006, **424**, 146.
13. S. Paolini, S. Fantoni, S. Moroni and S. Baroni, *J. Chem. Phys.*, 2005, **123**, 114306.
14. M. J. Weida, J. M. Sperhac, D. J. Nesbitt and J. M. Hutson, *J. Chem. Phys.*, 1994, **101**, 8351.
15. R. J. Le Roy, Y. Huang and C. Jary, *J. Chem. Phys.*, 2006, **125**, 164310.
16. R. J. Le Roy and R. D. E. Henderson, *Mol. Phys.*, 2007, **105**, 663.
17. G. Guelachvili, *J. Mol. Spectrosc.*, 1980, **79**, 72.
18. K. Raghavachari, J. A. P. G. W. Trucks and M. Head-Gordon, *Chem. Phys. Lett.*, 1989, **157**, 479.
19. D. E. Woon and T. H. Dunning, *J. Chem. Phys.*, 1993, **98**, 1358.
20. F. M. Tao and Y. K. Pan, *Mol. Phys.*, 1994, **81**, 507.
21. T. B. Pedersen, B. Fernandez, H. Koch and J. Makarewicz, *J. Chem. Phys.*, 2001, **115**, 8431.
22. S. F. Boys and F. Bernardi, *Mol. Phys.*, 1970, **19**, 553.
23. H.-J. Werner, P. J. Knowles, R. Lindh, F. R. Manby, M. Schütz, P. Celani, T. Korona, G. Rauhut, R. D. Amos, A. Bernhardsson, A. Berning, D. L. Cooper, M. J. O. Deegan, A. J. Dobbyn, F. Eckert, C. Hampel, G. Hetzer, A. W. Lloyd, S. J. McNicholas, W. Meyer, M. E. Mura, A. Nicklass, P. Palmieri, R. Pitzer, U. Schumann, H. Stoll, A. J. Stone, R. Tarroni and T. Thorsteinsson, *MOLPRO, version2006.1, a package of* ab initio *programs*, see http://www.molpro.net.
24. D. Q. Xie, H. Ran and Y. Z. Zhou, *Int. Rev. Phys. Chem.*, 2007, **26**, 487.
25. Y. Z. Zhou, D. Q. Xie and D. H. Zhang, *J. Chem. Phys.*, 2006, **124**, 144317.
26. H. Ran, Y. Zhou and D. Q. Xie, *J. Chem. Phys.*, 2007, **126**, 204304.
27. R. J. Le Roy and J. van Kranendonk, *J. Chem. Phys.*, 1964, **61**, 4750.
28. R. J. Le Roy and J. S. Carley, in *Potential Energy Surfaces of Adv. Chem. Phys.*, ed. K Lawley, John Wiley & Sons Ltd., New York, 1980, pp. 353–420.
29. R. J. Le Roy and J. M. Hutson, *J. Chem. Phys.*, 1987, **86**, 837.
30. H. Wei, R. J. Le Roy, R. Wheatley and W. J. Meath, *J. Chem. Phys.*, 2005, **122**, 084321.
31. B. R. Johnson and W. P. Reinhardt, *J. Chem. Phys.*, 1986, **85**, 4538.
32. S. E. Choi and J. C. Light, *J. Chem. Phys.*, 1990, **92**, 2129.
33. B. T. Sutcliffe and J. Tennyson, *Int. J. Quantum Chem.*, 1991, **39**, 183.
34. G. Audi, A. H. Wapstra and C. Thibault, *Nucl. Phys. A*, 2003, **729**, 337.
35. J. C. Light, I. P. Hamilton and J. V. Lill, *J. Chem. Phys.*, 1985, **82**, 1400.
36. C. Lanczos, *J. Res. Natl. Bur. Stand.*, 1950, **45**, 255.
37. J. M. Hutson, A. Ernesti, M. M. Law, C. F. Roche and R. J. Wheatley, *J. Chem. Phys.*, 1996, **105**, 9130.
38. A. Kumar and W. J. Meath, *Mol. Phys.*, 1985, **54**, 823.
39. B. L. Jhanwar and W. J. Meath, *Chem. Phys.*, 1982, **67**, 185.
40. A. Haskopoulos and G. Maroulis, *Chem. Phys. Lett.*, 2006, **417**, 235.
41. R. T. Park, *J. Chem. Phys.*, 1976, **64**, 1659.
42. R. J. Le Roy, *phiFIT 1.1: A Computer Program to Fit Potential Function Points to Selected Analytic Functions*, University of Waterloo Chemical Physics Research Report CP-663R (2006); see http://leroy.uwaterloo.ca/programs/.
43. R. J. Le Roy, *J. Mol. Spectrosc.*, 1998, **191**, 223.
44. Y. Xu and W. Jäager, *J. Mol. Struct.*, 2001, **599**, 211.
45. A. R. W. McKellar, *J. Chem. Phys.*, 2006, **125**, 114310.
46. J. Hepburn, G. Scoles and R. Penco, *Chem. Phys. Lett.*, 1975, **36**, 451.
47. R. Ahlrichs, R. Penco and G. Scoles, *Chem. Phys.*, 1977, **19**, 119.
48. C. Douketis, G. Scoles, S. Marchetti, M. Zen and A. J. Thakkar, *J. Chem. Phys.*, 1982, **76**, 3057.
49. K.-C. Ng, W. J. Meath and A. R. Allnatt, *Chem. Phys.*, 1978, **32**, 175.
50. K.-C. Ng, W. J. Meath and A. R. Allnatt, *Mol. Phys.*, 1979, **37**, 237.
51. K. T. Tang and J. P. Toennies, *J. Chem. Phys.*, 1977, **66**, 1496.
52. K. T. Tang and J. P. Toennies, *J. Chem. Phys.*, 1984, **80**, 3726.
53. M. B. E. Aguir, M. Y. Perrin and J. Taine, *J. Mol. Spectrosc.*, 2002, **215**, 234.
54. R. Bukowski, J. Saddlej, B. Jeziorski, P. Jankowski, K. Szalewicz, S. A. Kucharski, H. L. Williams and B. M. Rice, *J. Chem. Phys.*, 1999, **110**, 3785.
55. R. R. Toczylowski and F. D. S. M. Cybulski, *J. Chem. Phys.*, 2001, **114**, 851.
56. Y. Sumiyoshi and Y. Endo, *J. Chem. Phys.*, 2007, **127**, 184309.
57. A. Shayesteh, R. D. E. Henderson, R. J. Le Roy and P. F. Bernath, *J. Phys. Chem. A*, 2007, **111**, 12495.